Electric Sail displaced orbit control with solar wind uncertainties

Lorenzo Niccolai, Alessandro Anderlini, Giovanni Mengali, Alessandro A. Quarta[*]

Department of Civil and Industrial Engineering, University of Pisa, I-56122 Pisa, Italy

Abstract

The working principle of the Electric Solar Wind Sail, an innovative propellantless propulsion system proposed in 2004, is based on the electrostatic interaction between a spinning grid of tethers, kept at a high positive potential, and the incoming ions from the solar wind. Similar to the well-known solar sail concept, the E-sail could simplify the feasibility of advanced (deep space) missions which would otherwise require a significative amount of propellant, if enabled by conventional thrusters. However, the intrinsic variability of the solar wind properties makes accurate trajectory tracking a difficult task, since the perturbations of the solar wind dynamic pressure have the same order of magnitude as their mean value. To circumvent such a problem, in a recent study the plasma dynamic pressure was modelled as a random variable with a gamma probability density function and the sail grid voltage was suggested to be varied as a function of the instantaneous value of the solar wind properties. The aim of this paper is to improve those results, by discussing a more accurate statistical model of the solar wind dynamic pressure, which is used in the numerical simulations to estimate the actual impact of the solar wind uncertainties on the spacecraft heliocentric trajectory. In particular, the paper proposes a control law that is able to accurately track a nominal, non-Keplerian orbit.

Keywords: Electric solar wind sail, propulsive acceleration uncertainty, solar wind statistical model, non-Keplerian orbit

Nomenclature

$\boldsymbol{a}$	=	propulsive acceleration vector, $[\mathrm{mm/s^2}]$
a_c	=	characteristic acceleration, $[\mathrm{mm/s^2}]$
C	=	center of displaced non-Keplerian orbit
d	=	error in distance, $[\mathrm{au}]$
f	=	probability density function
k_1, k_2	=	gamma distribution parameters
L	=	tether length, $[\mathrm{km}]$
M	=	dimension of $\boldsymbol{\xi}$
m	=	spacecraft mass, $[\mathrm{kg}]$
N	=	number of tethers
n	=	number of simulations
$\hat{\boldsymbol{n}}$	=	normal unit vector
O	=	Sun's center of mass
P	=	order of sum
p	=	solar wind dynamic pressure, $[\mathrm{nPa}]$
R	=	random process

[*]Corresponding author

Email addresses: `lorenzo.niccolai@ing.unipi.it` (Lorenzo Niccolai), `alessandro.anderlini@ing.unipi.it` (Alessandro Anderlini), `g.mengali@ing.unipi.it` (Giovanni Mengali), `a.quarta@ing.unipi.it` (Alessandro A. Quarta)

$\boldsymbol{r}$	$=$	spacecraft position vector (with $r \triangleq \|\boldsymbol{r}\|$ and $\hat{\boldsymbol{r}} \triangleq \boldsymbol{r}/r$), [au]
$r_{\oplus L_1}$	$=$	Earth-L_1 distance, [au]
S	$=$	spacecraft center of mass
TS	$=$	T-score
T	$=$	total flight time, [years]
t	$=$	time, [days]
V	$=$	grid electric voltage, [kV]
V_{w}	$=$	solar wind electric potential, [kV]
$\boldsymbol{v}$	$=$	spacecraft velocity vector, [km/s]
w	$=$	weighting function
α	$=$	E-sail thrust angle, [deg]
α_n	$=$	E-sail pitch angle, [deg]
Γ	$=$	gamma function
ϵ	$=$	dimensionless error
ϵ_0	$=$	vacuum permittivity, [F/m]
θ	$=$	polar angle, [deg]
λ	$=$	Galerkin's projection coefficient
$\mu_\odot$	$=$	Sun's gravitational parameter, [km^3/s^2]
$\mu_\oplus$	$=$	Earth's gravitational parameter, [km^3/s^2]
$\boldsymbol{\xi}$	$=$	random vector
ρ	$=$	radius of circular displaced non-Keplerian orbit, [au]
σ	$=$	specific thrust, see Eq. (4), [N/m]
τ	$=$	switching parameter
Ψ_j	$=$	jth generalized polynomial basis
ψ	$=$	elevation angle, [deg]
Ω	$=$	parameter space
ω	$=$	angular velocity of displaced non-Keplerian orbit, [rad/year]
ω_K	$=$	Keplerian orbit angular velocity, [rad/year]

Subscripts

1	$=$	refined probability density function
2	$=$	gamma probability density function
gPC	$=$	generalized Polynomial Chaos
H	$=$	heliostationary condition
i	$=$	generic time step
j	$=$	polynomial basis index
k	$=$	generic summation index
L	$=$	artificial Lagrangian point
max	$=$	maximum allowable value
req	$=$	required value
st	$=$	maximum step variation
$\oplus$	$=$	value at $r = 1$ au

Superscripts

$-$	$=$	mean or nominal value
$\cdot$	$=$	time derivative
$\wedge$	$=$	unit vector

1. Introduction

The Electric Solar Wind Sail (E-sail) is a propellantless low-thrust propulsion system whose invention by Pekka Janhunen dates back to 2004 [1, 2]. It basically consists of a spinning grid of electrostatically

charged tethers, which are stretched by the centrifugal force, and maintained at a high potential by a power source. When an E-sail is immersed into the solar wind plasma, it generates a propulsive acceleration by exchanging momentum with the incoming ions. Possible mission scenarios that exploit an E-sail-induced thrust include deep space transfers to planets [3] or asteroids [4, 5, 6], generation of non-Keplerian orbits [7, 8], maintenance of artificial Lagrangian points [9, 10], and even more interesting options, such as manned Mars operations [11], outer Solar System exploration [12, 13, 14] and interstellar missions [15]. A derivation of the E-sail working principle, the plasma brake concept [16, 17], could be used to deorbit a spacecraft from a low Earth orbit.

The first plasma brake test was attempted with the Estonian satellite EstCube-1 [18], but a failure occurred to the tether unreel mechanism due to launch vibrational loads and the experiment failed [19]. Hopefully, the first *in-situ* test of plasma brake technology will be performed by the Finnish satellite Aalto-1 [20], which is equipped with a single 100 m-long tether. An encouraging result of the plasma brake experiment could lead to an operational test of the basic E-sail concept, which would require a mission outside Earth's magnetosphere.

The trajectory covered by a spacecraft propelled by an E-sail is usually estimated with a simplified approach based on two main hypotheses: 1) the E-sail is a perfectly flat and axially-symmetric body, and 2) the solar wind properties are both independent of the spacecraft position and time. Under these assumptions, the propulsive acceleration vector can be calculated as a function of the (constant) plasma dynamic pressure, the Sun-spacecraft distance, the E-sail attitude, and the grid voltage [21]. Accordingly, the E-sail trajectory can be obtained by numerically integrating the equations of motion, or by introducing some further simplifying hypotheses that allow an analytical closed-form expression of the propelled trajectory to be written [22, 23]. An in-depth discussion of the implications related to the first assumption may be found in Refs. [24, 25], which show that the effects of the tether inflection on the generated thrust are actually small. On the other hand, the second assumption has an inherent flaw, since the plasma properties are highly fluctuating and unpredictable, as reported by *in-situ* measurements provided by spacecraft in heliocentric orbits [26, 27, 28]. This makes an accurate trajectory tracking very difficult to obtain [29].

The impact of the solar wind uncertainties on the motion of a spacecraft equipped with an E-sail has been preliminarily studied by Toivanen and Janhunen [30], who proposed an approach based on performing a number of simulations based on historical data from different time intervals. More recently, the same topic was analyzed at length with a different method by Niccolai et al. [31], who proposed a statistical approach to model the solar wind dynamic pressure as a random variable with a suitable Probability Density Function (PDF). The latter was selected as a compromise solution between accuracy and simplicity, since the model derived from the available data requires a handy software implementation for obtaining numerical simulations. With this in mind, a gamma PDF was chosen due to its positive asymmetry, with shape and scale parameters selected such as to match the mean value and the standard deviation of the experimental measurements.

The aim of this paper is to improve the results of Refs. [31], by presenting a more accurate statistical model of the solar wind dynamic pressure, based on a PDF that is reconstructed from real data, with the aim of investigating the possibility of tracking a nominal trajectory through a grid-voltage control law. The obtained results are then compared with those of Ref. [31], and statistical tests are performed to evaluate whether the differences are significant in a preliminary mission phase.

This paper is organized as follows. First, the equations describing the orbital dynamics of an E-sail-based spacecraft are presented, and an accurate statistical model of the solar wind dynamic pressure is discussed. Then, in analogy with Ref. [31], a simulation is performed using a generalized Polynomial Chaos (gPC) procedure [32], to evaluate the impact of the solar wind uncertainties (modelled with the refined approach) on the E-sail trajectory. Finally, the most effective control law of Ref. [31], based on the concept of adjusting the E-sail grid voltage as a function of the instantaneous (local) value of the solar wind dynamic pressure, is tested with the new model. The results are compared with those obtained in Ref. [31] by means of statistical tests, in order to understand if the conclusions presented in the recent literature still hold. The conclusion section resumes the main outcomes of this work.

2. E-sail heliocentric dynamics

Consider a spacecraft S whose primary propulsion system is an E-sail, which covers a heliocentric (closed) orbit around the Sun's center-of-mass O. The spacecraft equations of motion can be written in a heliocentric-ecliptic inertial reference frame as

$$\dot{\boldsymbol{r}} = \boldsymbol{v} \tag{1}$$

$$\dot{\boldsymbol{v}} = -\frac{\mu_\odot}{r^3}\,\boldsymbol{r} + \boldsymbol{a} \tag{2}$$

where $\boldsymbol{r}$ is the spacecraft position vector (with $r \triangleq \|\boldsymbol{r}\|$), $\boldsymbol{v}$ is the spacecraft velocity vector, $\mu_\odot$ is the Sun's gravitational parameter, and $\boldsymbol{a}$ is the E-sail propulsive acceleration vector.

The characteristic acceleration a_c, that is, the maximum propulsive acceleration magnitude at a heliocentric distance $r = r_\oplus \triangleq 1\,\mathrm{au}$, is usually chosen as the E-sail performance parameter [33]. The value of a_c is a function of various E-sail design parameters such as the number of tethers N, the length L of each tether, and the total spacecraft mass m, that is [21]

$$a_c = \frac{N\,L\,\sigma_\oplus}{m} \tag{3}$$

where $\sigma_\oplus$ is the thrust per unit of tether length generated by the E-sail at a Sun-spacecraft distance equal to $r_\oplus$. According to Refs. [34, 35], $\sigma_\oplus$ is given by

$$\sigma_\oplus \triangleq 0.18 \max\left(0,\, V - V_\mathrm{w}\right)\sqrt{\epsilon_0\,p_\oplus} \tag{4}$$

where V is the grid voltage, $V_\mathrm{w} \simeq 1\,\mathrm{kV}$ is the electric potential of the solar wind ions, ϵ_0 is the vacuum permittivity, and $p_\oplus$ is the value of the plasma dynamic pressure at $r = r_\oplus$. Note that the typical value of V (a few tens of kilovolts) is significantly larger than that of V_w (about $1\,\mathrm{kV}$) [2], and so Eq. (4) reduces to

$$\sigma_\oplus = 0.18\,(V - V_\mathrm{w})\,\sqrt{\epsilon_0\,p_\oplus} \tag{5}$$

Using the geometrical model proposed by Huo et al. [21], and assuming a flat and axially-symmetric sail, the propulsive acceleration vector can be written as a function of a_c as

$$\boldsymbol{a} = \tau\,\frac{a_c}{2}\,\left(\frac{r_\oplus}{r}\right)\,[\hat{\boldsymbol{r}} + (\hat{\boldsymbol{r}} \cdot \hat{\boldsymbol{n}})\,\hat{\boldsymbol{n}}] \tag{6}$$

where $\tau \in \{0,\,1\}$ is a switching parameter, which accounts for the possibility of turning either on ($\tau = 1$) or off ($\tau = 0$) the E-sail electron gun, $\hat{\boldsymbol{r}} \triangleq \boldsymbol{r}/r$ is the radial unit vector, and $\hat{\boldsymbol{n}}$ is the unit vector normal to the E-sail nominal plane in the direction opposite to the Sun; see Fig. 1. The propulsive acceleration magnitude $a \triangleq \|\boldsymbol{a}\|$ is a function of the pitch angle α_n, defined as the angle between the directions of $\hat{\boldsymbol{n}}$ and $\hat{\boldsymbol{r}}$; see Fig. 2. Recalling Eq. (6), the solar wind uncertainties affect the propulsive acceleration only through a_c, which, according to Eqs. (3) and (5), is a function of the solar wind dynamic pressure at the Sun-Earth distance.

The usual deterministic approach for E-sail mission analysis consists of assuming $p_\oplus$ to be constant, which implies that its value is independent of both the spacecraft position $\boldsymbol{r}$ and the time instant t. The first assumption amounts to neglecting the variation of $p_\oplus$ with the heliocentric latitude which, according to Refs. [26, 36], is consistent with the actual solar wind behavior, provided the orbital inclination is not high or the spacecraft tracks a non-Keplerian orbit with constant latitude. However, the second assumption is not realistic, as will be discussed in the next subsection.

2.1. Statistical model of solar wind dynamic pressure

The time fluctuations of $p_\oplus$ do not show any regularity, although a weak periodicity related to the solar activity cycles may be identified. As such, the plasma dynamic pressure can be treated as a random variable, in accordance with the discussion by Meyer-Vernet [37]. This conservative assumption is justified by the fast and chaotic variations of $p_\oplus$, as reported by *in-situ* measurements, and amounts to take each value of $p_\oplus$ as independent of the previous ones.
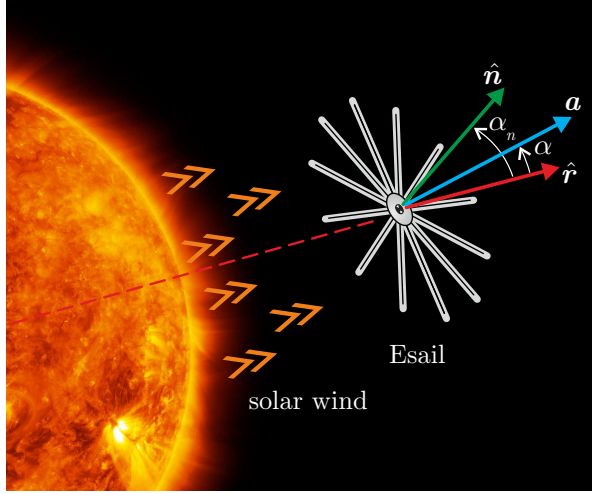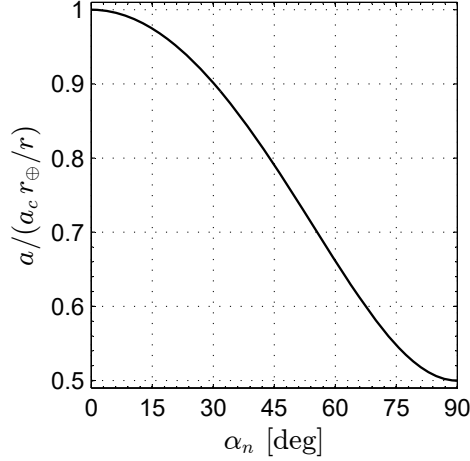
Figure 1: E-sail conceptual scheme.

Figure 2: Normalized E-sail propulsive acceleration magnitude a as a function of the sail pitch angle α_n.

Accordingly, in the numerical simulations of Ref. [31] the distribution of $p_\oplus$ was modelled as a gamma PDF, viz.

$$f(p_\oplus) = \frac{k_2^{-k_1}}{\Gamma(k_1)} \, p_\oplus^{k_1-1} \, \exp\left(-p_\oplus/k_2\right) \tag{7}$$

where $f(p_\oplus)\mathrm{d}p_\oplus$ denotes the probability that the solar wind dynamic pressure at the Sun-Earth distance ranges between $p_\oplus$ and $p_\oplus + \mathrm{d}p_\oplus$, and $\Gamma(x)$ is the gamma function of the generic variable x. The parameters $k_1 = 1.6437$ and $k_2 = 1.2168$ were chosen to fit the mean value and the standard deviation with the experimental data.

However, Eq. (7) does not ensure an accurate matching with experimental measurements. This is better appreciated with the aid of Fig. 3, which compares the gamma PDF with the histogram plot of the *in-situ* measurements of $p_\oplus$ from January 1996 to September 2013 taken from the NASA Omniweb database[1]. In particular, Fig. 3 confirms that the mean value of $p_\oplus$ is about $\overline{p}_\oplus = 2\,\mathrm{nPa}$, with a standard deviation of $1.56\,\mathrm{nPa}$ (note that in this work the bar symbol identifies either mean or nominal quantities), in accordance

---

[1]See `https://omniweb.gsfc.nasa.gov/form/dx1.html`. Retrieved on May 8, 2019.

with the values of k_1 and k_2 enforced in Eq. (7). Nevertheless, the gamma PDF overestimates the probability of having values of $p_\oplus$ smaller (or slightly greater) than $\overline{p}_\oplus$, while the peak in the vicinity of $\overline{p}_\oplus$ and the values of the tail are underestimated; see the zoom of Fig. 3.
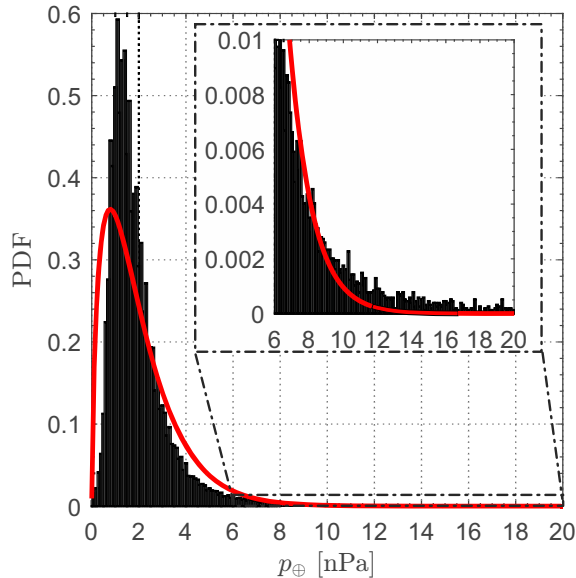

Figure 3: Comparison between the histogram plot of $p_\oplus$ measurements from January 1996 to September 2013 (bars) with the gamma PDF given by Eq. (7) (solid red line).

Based on the previous considerations, the statistical properties of $p_\oplus$ are now modelled with a more accurate distribution, obtained by available data, which allows its PDF to be accurately reconstructed.

2.2. Uncertainty Model

A generalized Polynomial Chaos (gPC) analysis [32] has been used to model the uncertainties related to the solar wind dynamic pressure. The approach consists in a spectral projection of a random process R over an orthogonal polynomial basis, which may be formally written as

$$R = \sum_{j=0}^{\infty} \lambda_j \Psi_j(\boldsymbol{\xi}) \tag{8}$$

where Ψ_j is the jth gPC polynomial basis and λ_j is its Galerkin's projection coefficient. Moreover, $\boldsymbol{\xi}$ is an M-dimensional random vector, defined in the parameter space Ω, which contains all of the uncertainties. In this work $M = 1$ (i.e., the random variable is a scalar ξ), because the only uncertain variable is assumed to be $p_\oplus$. For practical purposes the infinite sum in Eq. (8) is truncated at order P, so that the gPC expression reduces to

$$R = \sum_{j=0}^{P} \lambda_j \Psi_j(\xi) \tag{9}$$

Each coefficient λ_j is obtained using the orthogonality property of the polynomial basis, which leads to

$$\lambda_j = \frac{\langle R, \Psi_j \rangle}{\langle \Psi_j, \Psi_j \rangle} \tag{10}$$

where $\langle u, g \rangle$ represents the inner product between the two generic functions u and g, that is

$$\langle g, u \rangle = \int_\Omega u(\xi)\, g(\xi)\, w(\xi)\, \mathrm{d}\xi \tag{11}$$

6

In particular, the expansion (9) has been truncated at order $P = 4$, while each integral involved in the methodology has been computed though a Gaussian quadrature formula using $P + 1 = 5$ points. Each quadrature point defines a node at which the quantity of interest R must be sampled. As a result, the whole response surface can be reconstructed by means of $(P + 1)$ points only.

Returning to Eq. (11), it is worth noting that the two functions in the inner product are multiplied by a weighting function $w(\xi)$ associated to the orthogonal polynomial basis. A suitable polynomial family is thus characterized by a weighting function similar to the PDF shape of the input uncertainty ξ. For example, the set of generalized Laguerre polynomials is the typical choice when the input PDF is a gamma function. However, when the PDF cannot be well-reproduced by any of the Askey-Wiener families (uniform, gaussian, gamma, etc.), which are usually adopted in the gPC approach [32], an *ad-hoc* methodology must be introduced to construct an orthogonal basis. To that end, the procedure herein described follows the work of Margheri et al. [38]. Consider first the discrete PDF of the input uncertain parameter w_k

$$w_k^{\mathrm{norm}} = \frac{w_k}{\sum_{k=1}^{n_{\mathrm{int}}} \delta_{\mathrm{int}} w_k} \tag{12}$$

where w_k^{norm} is the normalized PDF, such that its integral is 1, while δ_{int} and n_{int} are the span and the number of intervals, respectively. The bases $\Psi_j(\xi)$ of the gPC are obtained with the Gram-Schmidt orthogonalization procedure, recursively defined as

$$\Psi_j(\xi) = \xi^j - \sum_{k=0}^{j-1} \frac{\langle \xi^j, \Psi_k \rangle}{\langle \Psi_k, \Psi_k \rangle} \Psi_k(\xi) \qquad \text{with} \quad \Psi_0(\xi) = 1 \tag{13}$$

where $\Psi_j(\xi)$ denotes the basis of order j, which is then normalized dividing it by $\langle \Psi_j, \Psi_j \rangle^{0.5}$. The inner products in Eq. (13) are computed as

$$\langle f, u \rangle = \sum_{k=1}^{n_{\mathrm{int}}} f(\overline{\xi}_k) \, u(\overline{\xi}_k) \, w_k^{\mathrm{norm}} \, \delta_{\mathrm{int}} \tag{14}$$

where $\overline{\xi}_k$ are the centers of each PDF interval. Because the previous polynomial family is not standard in the gPC methodology, the nodes ξ_k and the weights h_k of the Gaussian quadrature approach must be recovered using the Christoffel-Darboux formula. The latter states that the $P + 1$ quadrature points are the zeros of the polynomial $\Psi_{P+1}(\xi)$, while the weights are calculated as

$$h_k = -\frac{A_{P+2}}{A_{P+1}} \frac{\langle \Psi_P, \Psi_P \rangle}{\Psi_{P+2}(\xi_k) \Psi'_{P+1}(\xi_k)} = -\frac{A_{P+2}}{A_{P+1}} \frac{1}{\Psi_{P+2}(\xi_k) \Psi'_{P+1}(\xi_k)} \tag{15}$$

where the simplification is due to the polynomial normalization procedure, A_j is the coefficient of ξ^j in Ψ_j and the prime symbol denotes a derivative.

The previously discussed procedure allows an artificial PDF of $p_\oplus$ to be reconstructed from experimental measurements and to match all the statistical properties of experimental data. In this respect, Tab. 1 compares the statistical properties of the PDF based on experimental measurements and those of the gamma PDF used in Ref. [31] with *in-situ* measurements reported in Fig. 3. It is clear that the statistical distribution of experimental data is identical to the artificially-reconstructed refined PDF, so the histogram plot of Fig. 3 traces out both the distributions. Since the refined PDF matches the experimental data more accurately than the gamma PDF, it is now used to perform stochastic simulations of an E-sail heliocentric trajectory in a reference mission scenario in order to quantify its dispersion. In accordance with Ref. [31], the test case refers to a Sun-facing E-sail with a nominal characteristic acceleration $\overline{a}_c = 0.2 \, \mathrm{mm/s}^2$, which departs from a circular heliocentric parking orbit with radius $r = r_\oplus$. This situation is sketched in Fig. 4, where θ is a polar angle measured counterclockwise from to the initial Sun-spacecraft line, and is consistent with a spacecraft that leaves the Earth's sphere of influence with zero hyperbolic excess velocity. In particular, a Sun-facing case models an E-sail fixed attitude with respect to an orbital reference frame with $\alpha_n \equiv 0$, that is, $\hat{\boldsymbol{n}} \equiv \hat{\boldsymbol{r}}$; see Fig. 1.

Note that the nominal value of the characteristic acceleration corresponds to the (constant) value of a_c calculated through Eqs. (3) and (5) with $p_\oplus = \overline{p}_\oplus$. Such a value of $\overline{a}_c$ could be obtained by a spacecraft

	in-situ data	gamma PDF	refined PDF
mean value [nPa]	2.00	2.00	2.00
std. dev. [nPa]	1.56	1.56	1.56
skewness	4.09	1.56	4.09
kurtosis	33.13	3.65	33.13

Table 1: Comparison between the statistical properties of *in-situ* measurements of $p_\oplus$ with those of the gamma PDF from Ref. [31] and the refined PDF.
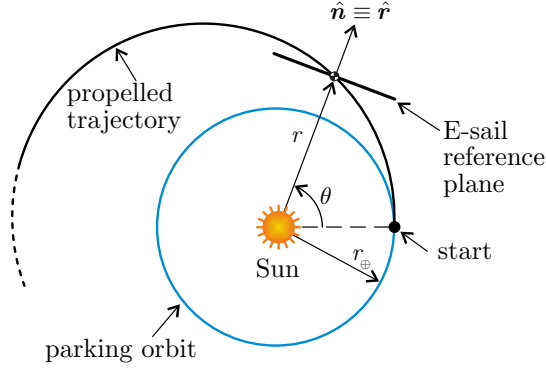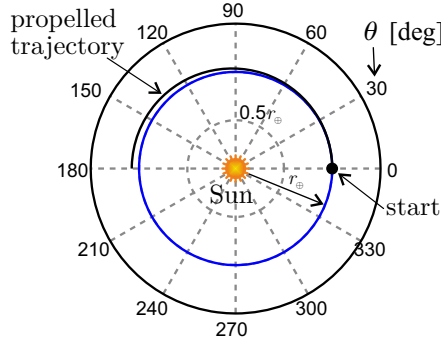

Figure 4: Sketch of the test case scenario.

Figure 5: Nominal trajectory of the test case scenario.

whose mass is $m = 560\,\text{kg}$, propelled by an E-sail with $N = 24$ tethers, each one being $L \simeq 8\,\text{km}$ long, and a nominal voltage $\overline{V} = 25\,\text{kV}$ [39]. Figure 5 shows the spacecraft nominal trajectory for $\theta \in [0, 180]\,\text{deg}$, which would be tracked if $p_\oplus \equiv \overline{p}_\oplus$ (and, consequently, $a_c \equiv \overline{a}_c$) during the whole flight time.

The previously described gPC procedure has been used to quantify the sensitivity of the spacecraft radial coordinate to the solar wind dynamic pressure, in order to compare the results obtained by modeling $p_\oplus$ with the gamma PDF with those given by the refined statistical model. In this context, Fig. 6 shows the approximate normalized PDF of $r = r(\theta)$ with $\theta \in [0, 180]\,\text{deg}$, obtained both with the refined PDF and the gamma PDF of Eq. (7). The darker lines denote more likely trajectories. Finally, Fig. 7 shows the estimated PDFs of $r(\theta)$ for $\theta = \{45, 90, 135, 180\}\,\text{deg}$ obtained by evaluating $p_\oplus$ with the refined model (black line) and the gamma PDF (red line). From both Figs. 6 and 7, it is evident that the trajectories associated with high probabilities are more concentrated in the vicinity of the nominal trajectory of Fig. 5, when the refined model is adopted. Note that the uncertainty on the spacecraft position is significant, even just after half a revolution around the Sun.

The interpolated PDF can be integrated to get the refined Cumulative Density Function (CDF) of $p_\oplus$,
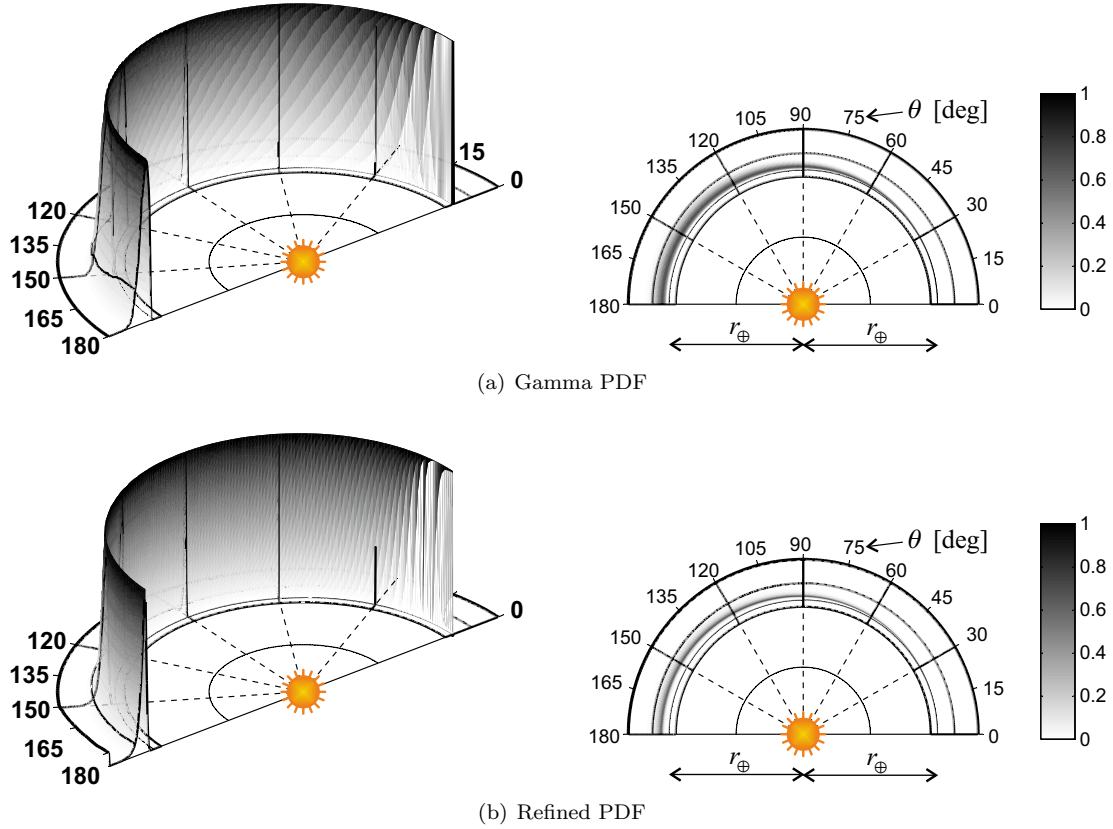
(a) Gamma PDF

(b) Refined PDF

Figure 6: Gamma PDF vs. refined PDF trajectory dispersion in the test case scenario.

which is compared in Fig. 8 with that obtained by the gamma distribution. The refined CDF data is used to generate random values of $p_\oplus$ with a statistical distribution that matches that of experimental data. From a practical point of view, the MATLAB built-in function `rand` is used to generate a random number between 0 and 1 (corresponding to a certain value of the CDF), which univocally identifies a point on the interpolated CDF plot. The abscissa of this point identifies the randomly generated value of $p_\oplus$.

3. Case study

Previous simulations [31] have shown that an accurate trajectory tracking with an E-sail is possible, provided that the spacecraft is equipped with a suitable control system. In the current analysis, the reference control law proposed in Ref. [31] will be tested with the previously described statistical model of the solar wind dynamic pressure. First, a brief review of the control law is given along with the simulation setup. For each mission case, the total flight time T is divided into legs of $0.01\,\mathrm{TU}_\odot = 0.58\,\mathrm{days} \simeq 14\,\mathrm{hours}$, in analogy with Ref. [31] and in accordance with *in-situ* measurements, which show significant fluctuations of solar wind properties that take place even in a few hours. At the time instant t_i, corresponding to the beginning of the $(i{+}1)$th leg, a random value of the solar wind dynamic pressure at the Sun-Earth distance $p_\oplus(t_i)$ is generated with the previous procedure, and is kept constant until the end of the leg. The spacecraft is assumed to be equipped with a particle detector (or an accelerometer) capable of measuring the instantaneous value of the local solar wind dynamic pressure $p(t)$. The measured value of $p(t)$ can be scaled to get $p_\oplus(t)$ from

$$p_\oplus(t) = p(t) \left(\frac{r}{r_\oplus} \right)^2 \tag{16}$$

The grid voltage is then adjusted as a function the instantaneous value of $p_\oplus(t_i)$. The rationale of the control law is to maintain the characteristic acceleration a_c as close as possible to its nominal value $\bar{a}_c$. Accordingly,
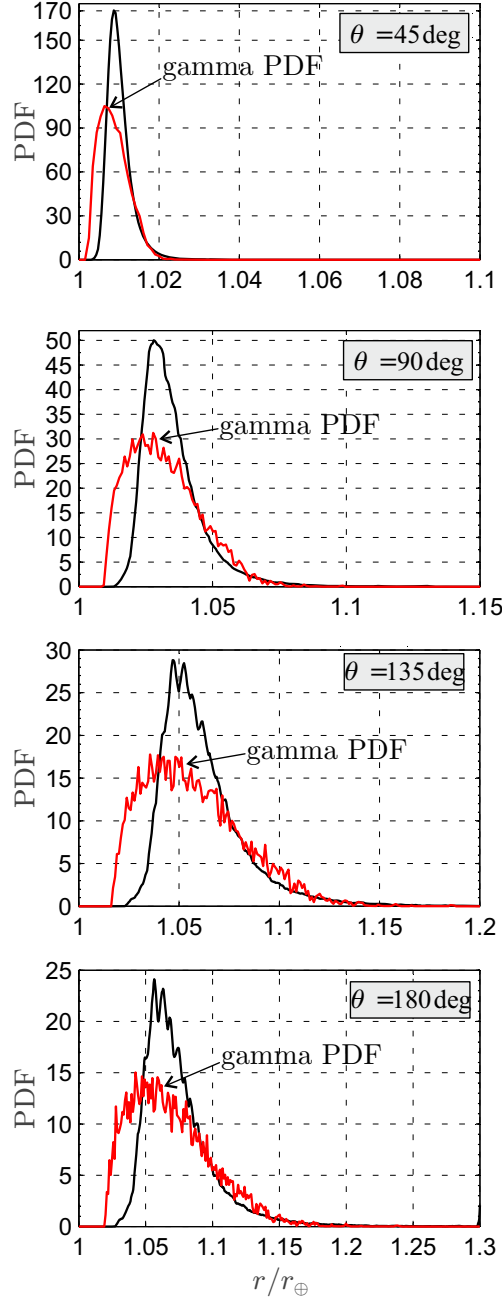
Figure 7: PDFs of $r = r(\theta)$ with $\theta = \{45, 90, 135, 180\}$ deg obtained with refined model of $p_\oplus$ (black line) and gamma PDF (red line).

the desired value of the grid voltage V_{req} at t_i is calculated as

$$V_{\mathrm{req}}(t_i) \triangleq V_{\mathrm{w}} + \frac{m\,\overline{a}_c}{0.18\,N\,L\,\sqrt{\epsilon_0\,p_\oplus(t_i)}} \equiv V_{\mathrm{w}} + \left(\overline{V} - V_{\mathrm{w}}\right)\,\sqrt{\frac{\overline{p}_\oplus}{p_\oplus(t_i)}} \tag{17}$$

where $\overline{V} = 25\,\mathrm{kV}$ is taken as the nominal value of the E-sail grid voltage [39]. Note that the required grid voltage V_{req} depends only on the nominal grid voltage $\overline{V}$ and on the instantaneous value of the solar wind dynamic pressure $p_\oplus(t_i)$ and, in particular, it is not an explicit function of other E-sail design characteristics, such as the number of tethers N, nor their length L.
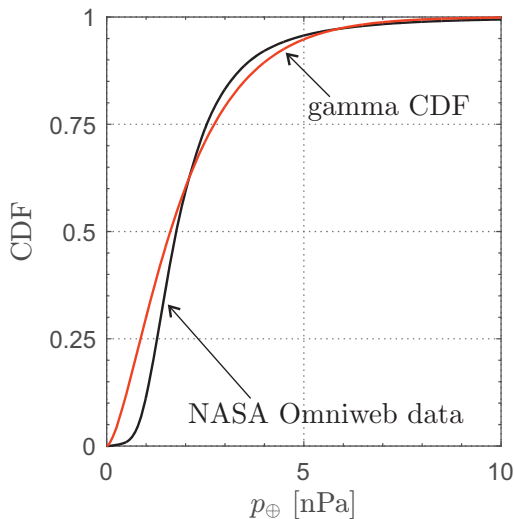
10

Figure 8: Comparison between the gamma CDF obtained from Eq. (7) (red line) with the CDF of $p_\oplus$ obtained from NASA Omniweb data (black line).

The control law tries to adjust the grid voltage at the beginning of each leg, in such a way that $V(t_i) = V_{\mathrm{req}}(t_i)$. However, it is realistic to assume that the voltage cannot exceed a maximum value and that the control system cannot instantaneously modify the grid voltage to reach the desired value. The first constraint is implemented in the model by introducing a maximum value V_{max} for the E-sail grid voltage. As long as the second constraint is concerned, it is assumed that, at the beginning of each leg, the voltage cannot be increased or decreased more than a given value V_{st} with respect to the previous leg. It is important to remark that preliminary calculations estimate that the typical characteristic time for an E-sail grid voltage adjustment is on the order of some minutes, thus very small when compared to the characteristic times of orbital dynamics. However, since experimental data are still lacking, and in analogy with previous studies [30, 31], this constraint has been conservatively included in the analysis. The two enforced constraints are both captured by the inequalities

$$V(t_i) \leq V_{\mathrm{max}} \tag{18}$$

$$|V(t_i) - V(t_{i-1})| \leq V_{\mathrm{st}} \tag{19}$$

To summarize, the control system adjusts the voltage $V(t_i)$ to the desired value $V_{\mathrm{req}}(t_i)$, calculated through Eq. (17), while enforcing the constraints (18) and (19). If $V_{\mathrm{req}}(t_i)$ does not comply with those constraints, the control system selects an admissible value $V(t_i)$ as close as possible to $V_{\mathrm{req}}(t_i)$. The whole control strategy is summarized in the flow chart of Fig. 9. Note that the control strategy described by Eqs. (17)–(19) assumes that the power consumption of the E-sail electron gun can be slightly adjusted. However, this hypothesis has a limited impact on the spacecraft dynamics. Indeed, according to the orbital motion limited (OML) current collection theory, the power consumption is proportional to the plasma number density and to $V^{3/2}$ [33, 40]. Therefore, if the power consumption is constrained to be constant, the grid voltage should be reduced when the plasma density increases, resulting in a very small variation of the generated thrust with respect to the previously described control law, and justifying the assumption. For an in-depth discussion of the control strategy the reader is referred to Ref. [31]. Once the voltage $V(t_i)$ is chosen, Eqs. (1)-(2) are integrated until the end of the $(i+1)$th leg, keeping the grid voltage and the plasma dynamic pressure constant, and using a variable order Adams-Bashforth-Moulton solver scheme [41, 42] with absolute and relative errors of 10^{-12}. Then, the procedure is restarted, until the total flight time T is reached.

This simulation setup has been used to test the control law of Eq. (17) in three potential E-sail-based mission scenarios. Different combinations of the pairs $\{V_{\mathrm{max}}, V_{\mathrm{st}}\}$ have been chosen and, for each combination, $n = 100$ numerical simulations have been completed. The effectiveness of the control law has been evaluated by means of a dimensionless error ϵ, to be later defined. A comparison has been made between
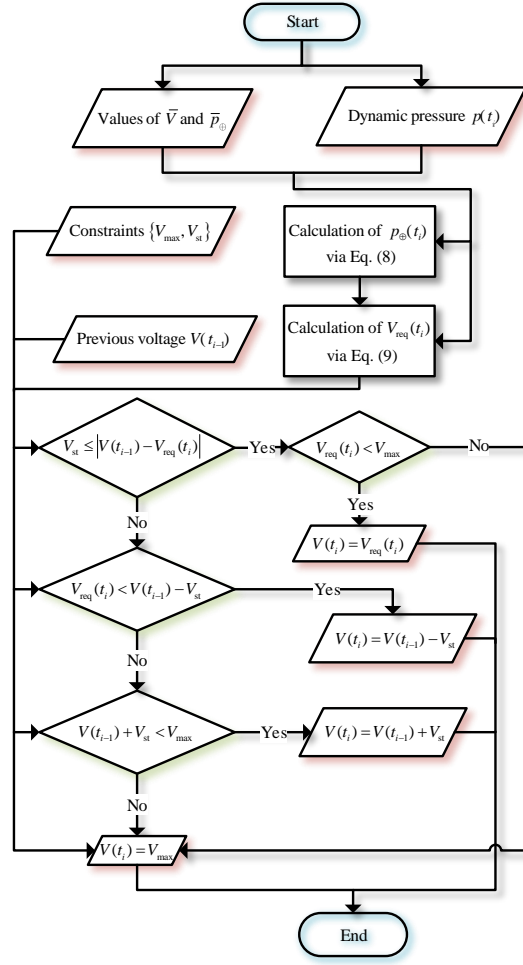
11

Figure 9: Flow chart of the grid voltage control law.

the results obtained when $p_\oplus$ has a PDF generated by the previous method (identified with subscript 1) and those (subscript 2) obtained with a gamma PDF, the latter being the same as that adopted in Ref. [31]. Note that, in principle, discrepancies between the numerical simulations performed with the two different PDFs could be related to the random generation of the values of $p_\oplus$. In order to understand whether the different results are caused by random fluctuations or by a statistically relevant difference between the two models, a T-score (TS) associated with the two samplings is defined as

$$\mathrm{TS} \triangleq \frac{|\bar{\epsilon}_1 - \bar{\epsilon}_2|}{\sqrt{\dfrac{\sigma_1^2 + \sigma_2^2}{n}}} \tag{20}$$

where $\bar{\epsilon}_1$ (or $\bar{\epsilon}_2$) is the mean value of the dimensionless error obtained with n simulations, while σ_1 (or σ_2) equals the corresponding standard deviation. The TS quantifies the probability for the difference between two samples (namely, the simulation outputs obtained with the gamma and the refined CDF), to be statistically relevant and not caused by random fluctuations. In practice, the confidence level corresponding to a given value of TS can be calculated from standard tables by recalling that the number of Degrees Of Freedom (DOF) is, in this case, $2\,n - 2 = 198$. Note that the calculation of TS with Eq. (20) assumes that the distributions of all possible samplings of $\bar{\epsilon}_1$ and $\bar{\epsilon}_2$ are both Gaussian. Since the sample dimensions are large ($n = 100$), this hypothesis is realistic. Finally, a sensitivity analysis focused on the length of the time leg is performed, comparing the outputs of previously described simulations (where a time leg of about 14 hours

is selected) with those obtained with a time leg of 6 hours or 1 day.

3.1. Case of heliostationary condition

The first mission case involves the maintenance of a heliostationary condition [7, 25, 43], that is, a mission that enables the continuous observation of the Sun's polar regions. Such a condition corresponds to when the Sun's gravitational pull equals the E-sail propulsive acceleration; see Fig. 10.
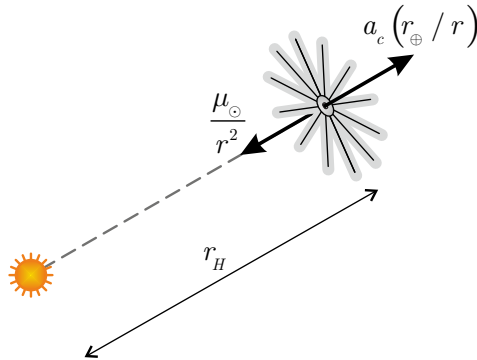

Figure 10: Sketch of the heliostationary mission scenario.

To maintain such an (unstable) equilibrium condition, the required value of the nominal characteristic acceleration $\bar{a}_c$ is

$$\bar{a}_c = \frac{\mu_\odot}{r_\oplus \, r_H} \tag{21}$$

where r_H is the levitation distance. Note that the propulsive acceleration must continuously operate on the spacecraft, that is $\tau \equiv 1$. Clearly, in this application the assumption of spatially-independent $p_\oplus$ is consistent, since the heliocentric latitude is fixed.

To get meaningful comparative results, the same mission scenario as that used in Ref. [31] has been simulated, that is, a heliostationary condition with $r_H = 1\,\mathrm{au}$. The latter requires a very high nominal characteristic acceleration ($\bar{a}_c = 5.93\,\mathrm{mm/s^2}$). The total simulated mission time is $T = 0.25\,\mathrm{years}$. Because in this case only radial forces are acting on the spacecraft, ϵ is taken equal to the dimensionless radial error, viz.

$$\epsilon \triangleq \frac{|r - r_H|}{r_H} \tag{22}$$

Table 2 shows the comparison between the results of Ref. [31] (subscript 2) and those obtained with the refined statistical model of $p_\oplus$ discussed here (subscript 1), for different combinations of the constraints $\{V_{\max}, V_{\mathrm{st}}\}$. The table reports the mean and maximum values of ϵ obtained with Eq. (22) and the values of TS given by Eq. (20).

3.2. Artificial Lagrangian point maintenance

The second mission scenario here addressed is the generation of an artificial collinear Lagrange point in the Sun-Earth gravitational field [9, 10]; see Fig. 11. This situation corresponds to a special case of non-Keplerian orbit with zero displacement with respect to the ecliptic plane. Such a mission is useful for solar observation purposes, and may be used to provide an early warning in case of solar events. The concept is similar to that of ACE mission [27], which, since 1997, is covering a Halo orbit around L_1 at an Earth-spacecraft distance $r_{\oplus L_1} \simeq 0.01\,\mathrm{au}$. The nominal heliocentric orbit requires the spacecraft to maintain an equilibrium condition when subjected to the Sun's and Earth's gravitational attractions, the centrifugal force, and the E-sail propulsive acceleration ($\tau \equiv 1$). Assuming that the barycenter of the Sun-Earth system coincides with the Sun's center of mass, the equilibrium point is at a Sun-spacecraft distance r_L given by

$$-\frac{\mu_\odot}{r_L^2} + \frac{\mu_\oplus}{r_{\oplus L_1}^2} + \bar{a}_c \left(\frac{r_\oplus}{r_L}\right) + \frac{\mu_\odot}{r_\oplus^3}\, r_L = 0 \tag{23}$$

13

V_{max} [kV]	V_{st} [kV]	Refined CDF		Gamma CDF		TS
		$\bar{\epsilon}_1$	$\max(\epsilon_1)$	$\bar{\epsilon}_2$	$\max(\epsilon_2)$	(198 DOF)
40	1	2.305	14.873	1.699	14.418	3.630
	5	1.501	12.515	1.227	11.227	2.271
	10	0.708	10.545	1.138	9.807	4.174
	40	0.556	4.180	2.655	14.266	27.019
60	1	2.409	15.049	1.758	24.986	3.822
	5	1.668	12.939	1.086	13.377	4.531
	10	0.948	11.159	1.141	12.767	1.573
	60	0.057	1.018	0.763	5.428	20.883
80	1	2.507	19.247	1.854	14.915	3.514
	5	1.637	14.094	1.320	12.933	2.357
	10	0.809	9.243	0.907	8.377	1.151
	80	0.031	0.738	0.348	2.906	12.214
no control		2.327	18.499	3.868	25.381	7.379

Table 2: Results for ϵ of the heliostationary mission simulations.
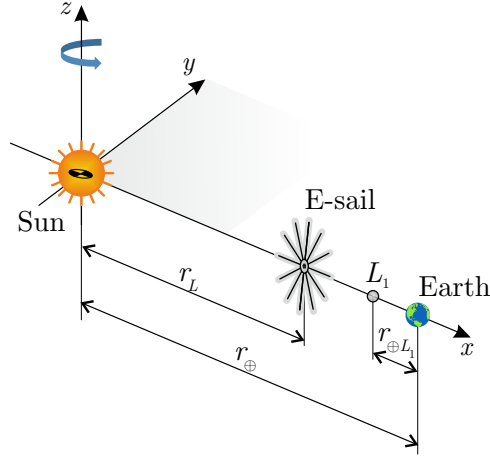

Figure 11: Sketch of the artificial Lagrangian point mission scenario.

where $\mu_\oplus$ is the Earth's gravitational parameter. Since in this case the spacecraft always lies on the ecliptic plane, the hypothesis of constant heliocentric latitude is satisfied.

The test case is similar to that of Ref. [31], and involves an E-sail-based spacecraft initially placed at $\bar{r} = r_L$ with an orbital period of 1 year, in such a way that the Sun, the spacecraft, and the Earth are constantly aligned; see Fig. 11. The E-sail nominal characteristic acceleration is $\bar{a}_c = 1\,\mathrm{mm/s^2}$, and the equilibrium radius, given by Eq. (23), is $r_L = 0.9436$ au. Such a value could guarantee a warning time of about 5.5 hours, whereas that of ACE mission amounts to about 1 hour. The simulated flight time is $T = 10$ years.

In this case, the most important requirement is the maintenance of the correct radial distance, whereas a misalignment with the Earth could be tolerated. Therefore, and in analogy with Ref. [31], the dimensionless error is defined as

$$\epsilon \triangleq \frac{|r - r_L|}{r_L} \tag{24}$$

The resulting mean and maximum values of ϵ, provided by Eq. (24), are listed in Tab. 3, along with the T-scores calculated with Eq. (20), for each different combination of the constraints $\{V_{max}, V_{st}\}$.

14

$V_{\max}$ [kV]	V_{st} [kV]	Refined CDF		Gamma CDF		TS
		$\bar{\epsilon}_1$	$\max(\epsilon_1)$	$\bar{\epsilon}_2$	$\max(\epsilon_2)$	(198 DOF)
40	1	2.411	13.337	2.418	14.660	0.082
	5	1.783	10.356	1.781	11.863	0.034
	10	1.328	8.691	1.526	8.385	4.000
	40	1.053	3.240	1.774	8.044	34.617
60	1	2.351	13.125	2.483	16.001	1.375
	5	1.931	10.657	2.199	14.218	3.180
	10	1.399	6.164	1.821	11.480	7.087
	60	0.878	2.154	1.131	4.143	101.242
80	1	2.471	14.526	2.399	16.306	0.717
	5	1.801	10.086	1.994	14.941	2.827
	10	1.482	9.147	1.850	11.519	5.760
	80	0.757	1.737	1.008	3.119	21.024
no control		2.263	14.906	2.899	8.071	6.364

Table 3: Results for ϵ of the artificial Lagrangian point maintenance simulations.

3.3. Displaced non-Keplerian orbit

The last mission case is a circular heliocentric Displaced Non-Keplerian Orbit (DNKO). The orbital plane of a DNKO does not include the primary's center of mass [44, 45], therefore such orbit is to be maintained with a continuous propulsive acceleration ($\tau \equiv 1$) that balances the Sun's gravitational attraction and the centrifugal force; see Fig. 12.

Confining the study to circular DNKOs, these orbits are univocally defined by three parameters, that is, $\{\rho, \psi, \omega_K\}$ where ρ is the distance between the spacecraft and the projection of O on the orbital plane, ψ is the elevation angle from the ecliptic plane to the position vector $\boldsymbol{r}$, and $\omega_K \triangleq \sqrt{\mu_\odot/r^3}$ is the reference angular velocity. The equations required for orbital maintenance are [7]

$$\alpha = \arctan\left[\frac{(\omega/\omega_K)^2 \tan\psi}{1 + \tan^2\psi - (\omega/\omega_K)^2}\right] \tag{25}$$

$$\bar{a}_c = \frac{2\,\mu_\odot \cos\psi}{r_\oplus\,\rho\,\sqrt{1 + 3\cos^2\alpha_n}}\left|1 - \frac{(\omega/\omega_K)^2}{1 + \tan^2\psi}\right|\sqrt{1 + \frac{\tan^2\psi}{[(1+\tan^2\psi)/(\omega/\omega_K)^2 - 1)]^2}} \tag{26}$$

where α is the angle between the radial unit vector $\hat{\boldsymbol{r}}$ and the propulsive acceleration vector $\boldsymbol{a}$; see Fig. 12. According to the thrust model discussed in Ref. [21], the maximum value of α that can be generated by an E-sail is about 19.47 deg, which represents a constraint for physically feasible DNKOs. The test case involves an E-sail in a circular DNKO with $\rho = 0.99$ au, $\psi = 0.57$ deg, and $\omega_K = 2\pi$ rad/year, corresponding to a spacecraft that levitates above the ecliptic plane at 99% of the Sun-Earth distance, with the same orbital period as the Earth. For the sake of simplicity, the Earth's orbital eccentricity is here neglected, and so is its gravitational attraction, since the spacecraft is always far outside the planetary sphere of influence. Note that a circular DNKO complies with the hypothesis of constant heliocentric latitude. The required nominal characteristic acceleration is $\bar{a}_c = 0.2349$ mm/s^2, given by Eq. (26).

In a DNKO mission scenario, it is important that the spacecraft be capable of tracking the nominal trajectory without significant deviations in any of the three spatial dimensions. To capture this requirement, the dimensionless error is defined as

$$\epsilon \triangleq d/\rho \tag{27}$$

where d is the distance between the nominal vectorial position of the spacecraft along its orbit and its actual vectorial position calculated with an orbital propagator. The situation is illustrated in Fig. 13. In analogy with the previous mission cases, the results in terms of ϵ (given by Eq. (27)) and the values of TS (see Eq. (20)) are reported in Tab. 4.
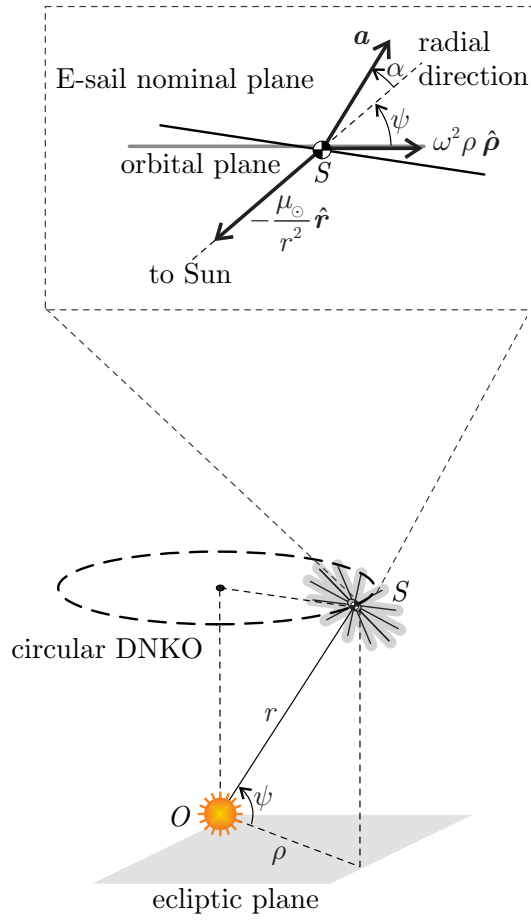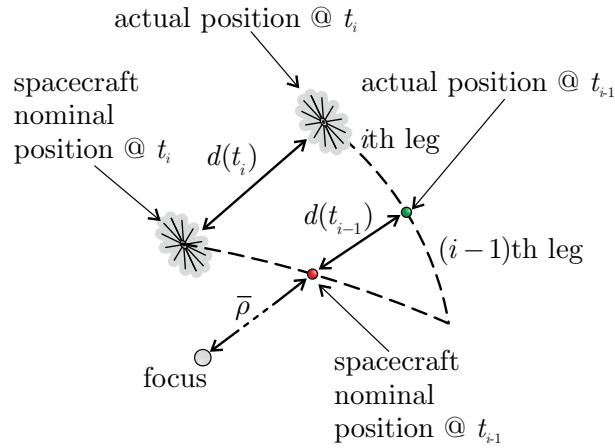
Figure 12: Sketch of the DNKO mission scenario.

Figure 13: Sketch of the quantities involved in the calculation of the dimensionless error ϵ.

3.4. Result analysis and discussion

The results reported in Tabs. 2–4 all share some common trends. First, the uncontrolled dynamics of an E-sail-based spacecraft cannot be accurately predicted, but the mean error obtained with the refined

$V_{\max}$ [kV]	V_{st} [kV]	Refined CDF		Gamma CDF		TS
		$\bar{\epsilon}_1$	$\max(\epsilon_1)$	$\bar{\epsilon}_2$	$\max(\epsilon_2)$	(198 DOF)
40	1	2.039	6.139	1.092	5.582	20.948
	5	1.221	4.047	0.454	2.424	23.773
	10	0.456	2.072	0.768	2.951	10.440
	40	0.410	1.293	2.120	5.394	83.412
60	1	2.014	6.655	1.080	4.800	17.876
	5	1.252	4.210	0.811	3.998	9.241
	10	0.648	2.472	0.526	3.007	3.814
	60	0.050	0.273	0.627	2.294	49.497
80	1	2.014	6.378	1.115	4.861	17.659
	5	1.275	4.385	0.812	3.913	11.126
	10	0.635	2.283	0.566	2.880	2.095
	80	0.018	0.167	0.261	0.949	34.745
no control		1.797	6.408	2.727	8.437	14.756

Table 4: Results for ϵ of the DNKO maintenance simulations.

CFD is slightly smaller than that with a gamma CFD in all of the analyzed cases. Such a difference is statistically relevant (see the TS column) with a confidence level greater than 99.9%, corresponding to a TS of about 3.34. This behavior confirms the result of the gPC simulations, which have shown that more likely trajectories are concentrated around the nominal one, as previously noted.

When the constraints are tight (i.e., both $V_{\max}$ and V_{st} are small), the estimated performance of the grid voltage control law with the refined PDF is slightly worse in comparison with the results of Ref. [31], but in some cases the TS is too small to ensure that these differences are statistically relevant. Indeed, a value of TS smaller than 0.68 implies that the differences between the dimensionless errors are statistically relevant with a probability below 50%. The only exception is the DNKO case, where the discrepancies between the two models seem to be more relevant, possibly due to the different definition of the dimensionless error ϵ, see Eq. (27). In this case, the performance worsening is probably due to the fact that occasional high values of $p_{\oplus}$ may occur in the refined model, which cannot be suitably counteracted by the control system when V_{st} is too small, thus significantly deviating the spacecraft from its nominal trajectory.

However, the most important results are those associated with high values of $\{V_{\max}, V_{\mathrm{st}}\}$, especially those with $V_{\mathrm{st}} = V_{\max}$, which essentially imply a removal of the constraint on V_{st}. This condition is fairly realistic, since, as already stated, preliminary calculations suggest that the constraint on the voltage variation quickness could possibly be relaxed or removed. Firstly, note that the combinations with large values of $V_{\max}$ and V_{st} are the only ones that allow the nominal trajectory to be tracked with a satisfying accuracy, as it was already noted in Ref. [31]. Moreover, in each case, the performance of the control system increases when the refined model of $p_{\oplus}$ is implemented, with a confidence level greater than 99.5%. This result is probably due to a larger positive asymmetry of the refined PDF compared to the gamma PDF, which implies that high (or very high) values of $p_{\oplus}$ are not as unlikely as they were in the simulations discussed in Ref. [31], whereas values smaller then $\bar{p}_{\oplus}$ are less probable; see Fig. 3. From a practical point of view, very small values of $p_{\oplus}$ should be counterbalanced by large values of the grid voltage, which could violate the saturation constraint expressed by $V_{\max}$. On the other hand, the occasional generation of very high values of $p_{\oplus}$ can be balanced by quickly reducing the grid voltage towards V_{w}, see Eq. (5), and this can be done (almost) instantaneously when the constraint on V_{st} is removed (or relaxed). This aspect could explain the better performance of the grid voltage control law obtained with the refined statistical model, when a large value of V_{st} is assumed.

3.5. Time-leg sensitivity analysis

In order to evaluate whether the choice of the time leg significantly influences the previously listed results, the numerical simulations of orbital maintenance in the three analyzed scenarios have been repeated with different lengths of the time leg. Table 5 compares the most promising outputs given by the previously discussed simulations with those obtained by maintaining the same values of the constraints $V_{\max}$ and V_{st},

but setting a time leg of 6 hours or 1 day. Note that the performance of the control law are not significantly affected by the choice of the time leg, in particular when a large value of V_{st} is assumed.

	V_{max} [kV]	V_{st} [kV]	0.58 days		6 hours		1 day	
			$\bar{\epsilon}_1$	$\max(\epsilon_1)$	$\bar{\epsilon}_1$	$\max(\epsilon_1)$	$\bar{\epsilon}_1$	$\max(\epsilon_1)$
Hel	40	40	0.556	4.180	0.508	3.030	0.507	5.187
	60	60	0.057	1.018	0.061	0.515	0.102	2.285
	80	10	0.809	9.243	0.683	6.264	0.912	11.831
	80	80	0.031	0.738	0.024	0.419	0.030	1.725
Lag	40	40	1.053	3.240	1.052	2.428	1.074	4.638
	60	60	0.878	2.154	0.885	1.732	0.879	2.245
	80	10	1.482	9.147	1.242	5.553	1.665	11.730
	80	80	0.757	1.737	0.783	1.584	0.732	1.922
DNKO	40	40	0.410	1.293	0.421	1.493	0.421	1.485
	60	60	0.050	0.273	0.051	0.497	0.051	0.369
	80	10	0.635	2.283	0.638	3.372	0.630	3.323
	80	80	0.018	0.167	0.016	0.232	0.014	0.203

Table 5: Time leg sensitivity analysis for the three analyzed mission scenario (Hel = heliostationary position, Lag = artificial Lagrangian point).

4. Conclusions

The impact of solar wind property fluctuations on the capability of an Electric Solar Wind Sail-based spacecraft to track a nominal trajectory has been preliminarily estimated. The analysis exploits a refined statistical model of the solar wind plasma dynamic pressure, based on a Probability Density Function reconstructed from *in-situ* experimental measurements, for improving the recent results available in the literature.

Numerical simulations have shown that the spacecraft dynamics is substantially affected and a suitable control system is therefore required to counterbalance the environmental fluctuations in a possible mission scenario. The proposed control law reduces that problem by adjusting the grid voltage as a function of the instantaneous value of the local solar wind dynamic pressure. The control law has been tested in three mission scenarios, and the results have been compared with those obtained by modeling the dynamic pressure with a classical gamma probability density function. A negligible performance worsening has been registered when the saturation voltage is small and the capability of quickly responding to environmental fluctuations is limited. However, when large saturation voltage and quick voltage variations are possible, the control system performance with the refined statistical model has shown a relevant improvement compared to that estimated with a gamma probability density function. This represents an interesting outcome, as it implies that a high performance control system could enable an Electric Solar Wind Sail-based spacecraft to track a nominal trajectory with a good accuracy level. Further developments of the analysis presented in this work could include the temporal correlation in the statistical model of the solar wind dynamic pressure, thus removing the assumption that its instantaneous value is unaffected by the previous ones.

References

[1] P. Janhunen, Electric sail for spacecraft propulsion, Journal of Propulsion and Power 20 (4) (2004) 763–764, doi: 10.2514/1.8580.

[2] P. Janhunen, A. Sandroos, Simulation study of solar wind push on a charged wire: basis of solar wind electric sail propulsion, Annales Geophysicae 25 (3) (2007) 755–767, doi: 10.5194/angeo-25-755-2007.

[3] M. Huo, G. Mengali, A. A. Quarta, Optimal planetary rendezvous with an electric sail, Aircraft Engineering and Aerospace Technology 88 (4) (2016) 512–522, doi: 10.1108/AEAT-01-2015-0012.

[4] A. A. Quarta, G. Mengali, Electric sail missions to potentally hazardous asteroids, Acta Astronautica 66 (9–10) (2010) 1506–1509, doi: 10.1016/j.actaastro.2009.11.021.

[5] G. Mengali, A. A. Quarta, Optimal nodal flyby with near-Earth asteroids using electric sail, Acta Astronautica 104 (2) (2014) 450–457, doi: 10.1016/j.actaastro.2014.02.012.

[6] K. Yamaguchi, H. Yamakawa, Electric solar wind sail kinetic energy impactor for asteroid deflection missions, Journal of the Astronautical Sciences 63 (1), doi: 10.1007/s40295-015-0081-x.

[7] L. Niccolai, A. A. Quarta, G. Mengali, Electric sail-based displaced orbits with refined thrust model, Proceedings of the Institution of Mechanical Engineers, Part G: Journal of Aerospace Engineering 232 (3) (2017) 423–432, doi: 10.1177/0954410016679195.

[8] L. Niccolai, A. A. Quarta, G. Mengali, Electric sail elliptic displaced orbits with advanced thrust model, Acta Astronautica 138 (2017) 503–511, doi: 10.1016/j.actaastro.2016.10.036.

[9] G. Aliasi, G. Mengali, A. A. Quarta, Artificial equilibrium points for an electric sail with constant attitude, Journal of Spacecraft and Rockets 50 (6) (2013) 1295–1298, doi: 10.2514/1.A32540.

[10] G. Vulpetti, C. Circi, T. Pino, Coronal Mass Ejection early-warning mission by solar-photon sailcraft, Acta Astronautica 140 (2017) 113–125, doi: 10.1016/j.actaastro.2017.07.042.

[11] P. Janhunen, S. Merikallio, M. Paton, EMMI-Electric solar wind sail facilitated Manned Mars Initiative, Acta Astronautica 113 (2015) 22–28, doi: 10.1016/j.actaastro.2015.03.029.

[12] G. Mengali, A. A. Quarta, P. Janhunen, Considerations of electric sailcraft trajectory design, JBIS-Journal of the British Interplanetary Society 61 (8) (2008) 326–329 .

[13] A. A. Quarta, G. Mengali, Electric sail mission analysis for outer Solar System exploration, Journal of Guidance, Control, and Dynamics 33 (3) (2010) 740–755, doi: 10.2514/1.47006.

[14] P. Janhunen, J.-P. Lebreton, S. Merikallio, M. Paton, G. Mengali, A. A. Quarta, Fast E-sail Uranus entry probe mission, Planetary and Space Science 104 (PA) (2014) 141–146, doi: 10.1016/j.pss.2014.08.004.

[15] N. Perakis, A. M. Hein, Combining magnetic and electric sails for interstellar deceleration, Acta Astronautica 128 (2018) 13–20, doi: 10.1016/j.actaastro.2016.07.005.

[16] P. Janhunen, Electrostatic plasma brake for deorbiting a satellite, Journal of Propulsion and Power 26 (2) (2010) 370–372, doi: 10.2514/1.47537.

[17] L. Orsini, L. Niccolai, G. Mengali, A. A. Quarta, Plasma brake model for preliminary mission analysis, Acta Astronautica 144 (2018) 297–304, doi: 10.1016/j.actaastro.2017.12.048.

[18] S. Lätt, A. Slavinskis, E. Ilbis, et al., ESTCube-1 nanosatellite for electric solar wind sail in-orbit technology demonstration, Proceedings of the Estonian Academy of Sciences 63 (2S) (2014) 200–209, doi: 10.3176/proc.2014.2S.01.

[19] A. Slavinskis, M. Pajusaku, H. Kuuste, et al., ESTCube-1 in-orbit experience and lessons learned, IEEE Aerospace and Electronic Systems Magazine 30 (8) (2015) 12–22, doi: 10.1109/MAES.2015.150034.

[20] O. Khurshid, T. Tikka, J. Praks, M. Hallikainen, Accomodating the plasma brake experiment on-board the Aalto-1 satellite, Proceedings of the Estonian Academy of Sciences 63 (2S) (2014) 258–266, doi: 10.3176/proc.2014.2S.07.

[21] M. Huo, G. Mengali, A. A. Quarta, Electric sail thrust model from a geometrical perspective, Journal of Guidance, Control, and Dynamics 41 (3) (2018) 734–740, doi: 10.2514/1.G003169.

[22] A. A. Quarta, G. Mengali, Trajectory approximation for low-performance electric sail with constant thrust angle, Journal of Guidance, Control, and Dynamics 36 (3) (2013) 884–887, doi: 10.2514/1.59076.

[23] L. Niccolai, A. A. Quarta, G. Mengali, Two-dimensional heliocentric dynamics approximation of an electric sail with fixed attitude, Aerospace Science and Technology 71 (2017) 441–446, doi: 10.1016/j.ast.2017.09.045.

[24] M. Bassetto, G. Mengali, A. A. Quarta, Thrust and torque vector characteristics of axially-symmetric E-sail, Acta Astronautica 146 (2018) 134–143, doi: 10.1016/j.actaastro.2018.02.035.

[25] M. Bassetto, G. Mengali, A. A. Quarta, Stability and control of spinning E-sail in heliostationary orbit, Journal of Guidance, Control, and Dynamics 42 (2) (2019) 425–431, doi: 10.2514/1.G003788.

[26] J. L. Phillips, S. J. Bame, A. Barnes, et al., Ulysses solar wind plasma observations from pole to pole, Geophysical Research Letters 22 (23) (1995) 3301–3304, doi: 10.1029/95GL03094.

[27] E. C. Stone, A. M. Frandsen, R. A. Mewaldt, E. R. Christian, D. Margolies, J. F. Ormes, F. Snow, The Advanced Composition Explorer, Space Science Reviews 86 (1–4) (1998) 1–22 .

[28] L. Gallana, F. Fraternale, M. Iovieno, S. M. Fosson, E. Magli, M. Opher, J. D. Richardson, D. Tordella, Voyager 2 solar plasma and magnetic field spectral analysis for intermediate data sparsity, Journal of Geophysical Research: Space Physics 121 (5) (2016) 3905–3919, doi: 10.1002/2015JA021830.

[29] G. Vulpetti, A critical review on the viability of a space propulsion based on the solar wind momentum flux, Acta Astronautica 32 (9) (1994) 641–644, doi: 10.1016/0094-5765(94)90074-4.

[30] P. K. Toivanen, P. Janhunen, Electric sailing under observed solar wind conditions, Astrophysics and Space Science Transactions 5 (1) (2009) 61–69, doi: 10.5194/astra-5-61-2009.

[31] L. Niccolai, A. Anderlini, G. Mengali, A. A. Quarta, Impact of solar wind fluctuations on electric sail mission design, Aerospace Science and Technology 82–83 (2018) 38–45, doi: 10.1016/j.ast.2018.08.032.

[32] D. Xiu, G. E. Karniadakis, The Wiener–Askey Polynomial Chaos for stochastic differential equations, SIAM J. Sci. Comput. 24 (2) (2003) 619–644, doi: 10.1137/S1064827501387826.

[33] G. Mengali, A. A. Quarta, P. Janhunen, Electric sail performance analysis, Journal of Spacecraft and Rockets 45 (1) (2008) 122–129, doi: 10.2514/1.31769.

[34] P. K. Toivanen, P. Janhunen, Spin plane control and thrust vectoring of electric solar sail by tether potential modulation, Journal of Propulsion and Power 29 (1) (2013) 178–185, doi: 10.2514/1.B34330.

[35] P. K. Toivanen, P. Janhunen, Thrust vectoring of an electric sail with a realistic sail shape, Acta Astronautica 131 (2017) 145–151, doi: 10.1016/j.actaastro.2016.11.027.

[36] J. M. Sokół, M. Bzowski, M. Tokumaru, K. Fujiki, D. J. McComas, Heliolatitude and time variations of solar wind structure from in situ measurements and interplanetary scintillation observations, Solar Physics 285 (1-2) (2013) 167–200, doi: 10.1007/s11207-012-9993-9.

[37] N. Meyer-Vernet, Basics of the Solar Wind, Cambridge University Press, 2007, Ch. 6, pp. 291–333.

[38] L. Margheri, M. Meldi, M. V. Salvetti, P. Sagaut, Epistemic uncertainties in RANS model free coefficients, Computers and Fluids 102 (2014) 315–335, doi: 10.1016/j.compfluid.2014.06.029.

[39] P. Janhunen, A. A. Quarta, G. Mengali, Electric solar wind sail mass budget model, Geoscientific Instrumentation, Methods and Data Systems 2 (1) (2013) 85–95, doi: 10.5194/gi-2-85-2013.

[40] P. K. Toivanen, P. Janhunen, J. Envall, Electric sail control mode for amplified transverse thrust, Acta Astronautica 106 (2015) 111–119, doi: 10.1016/j.actaastro.2014.10.031.

[41] L. F. Shampine, M. K. Gordon, Computer Solution of Ordinary Differential Equations: The Initial Value Problem, W. H. Freeman & Co Ltd, San Francisco, 1975, Ch. 10, ISBN: 0-716-70461-7.

[42] L. F. Shampine, M. W. Reichelt, The MATLAB ODE suite, SIAM Journal on Scientific Computing 18 (1) (1997) 1–22, doi: 10.1137/S1064827594276424.

[43] G. Mengali, A. A. Quarta, Optimal heliostationary missions of high-performance sailcraft, Acta Astronautica 60 (8-9) (2007) 676–683, doi: 10.1016/j.actaastro.2006.07.018.

[44] C. R. McInnes, Solar Sailing: Technology, Dynamics and Mission Applications, Springer-Verlag, 1999, Ch. 5, pp. 171–196.

[45] R. J. McKay, M. Macdonald, J. Biggs, C. R. McInnes, Survey of highly-non-Keplerian orbits with low-thrust propulsion, Journal of Guidance, Control, and Dynamics 34 (3) (2011) 645–666, doi: 10.2514/1.52133.